JACS
JOURNAL OF THE AMERICAN CHEMICAL SOCIETY
pubs.acs.org/JACS
Article

Exploiting Functional Impurities for Fast and Efficient Incorporation of Manganese into Quantum Dots

Ho Jin, Mateusz Goryca, Michael T. Janicke, Scott A. Crooker, and Victor I. Klimov*

Cite This: J. Am. Chem. Soc. 2020, 142, 18160−18173
Read Online

ABSTRACT: The incorporation of manganese (Mn) ions into Cd(Zn)-chalcogenide QDs activates strong spin-exchange interactions between the magnetic ions and intrinsic QD excitons that have been exploited for color conversion, sunlight harvesting, electron photoemission, and advanced imaging and sensing. The ability to take full advantage of novel functionalities enabled by Mn dopants requires accurate control of doping levels over a wide range of Mn contents. This, however, still represents a considerable challenge. Specific problems include the difficulty in obtaining high Mn contents, considerable broadening of QD size dispersion during the doping procedure, and large batch-to-batch variations in the amount of incorporated Mn. Here, we show that these problems originate from the presence of unreacted cadmium (Cd) complexes whose abundance is linked to uncontrolled impurities participating in the QD synthesis. After identifying these impurities as secondary phosphines, we modify the synthesis by introducing controlled amounts of "functional" secondary phosphine species. This allows us to realize a regime of nearly ideal QD doping when incorporation of magnetic ions occurs solely via addition of Mn−Se units without uncontrolled deposition of Cd−Se species. Using this method, we achieve very high per-dot Mn contents (>30% of all cations) and thereby realize exceptionally strong exciton-Mn exchange coupling with *g*-factors of ∼600.

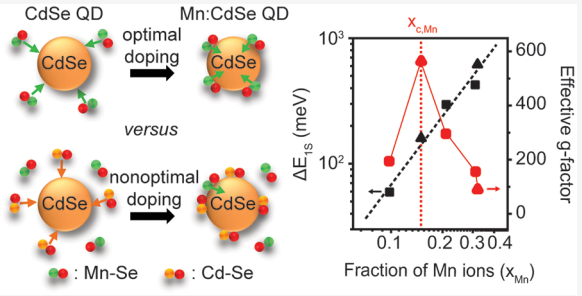

INTRODUCTION

The incorporation of paramagnetic, spin-5/2 manganese (Mn) impurities into II−VI colloidal quantum dots (QDs) results in considerable modifications of their optical and magneto-optical properties.[1−10] In particular, strong sp-d exchange interactions between a semiconductor host and magnetic impurities lead to fast excitation transfer from the QD to the Mn ions, which enables highly efficient emission in the intragap region due to radiative relaxation of the excited Mn state.[5,7,11−15] This process has been exploited for color conversion in light emitting devices[16−18] and sunlight harvesting in luminescent solar concentrators.[19,20] The spin-exchange Auger-type energy transfer from the excited Mn ions to QD excitons is also extremely fast (subpicosecond time scales[21]), which allows one to manipulate nonequilibrium "hot" unrelaxed carriers[21] and produce efficient photoemission with weak continuous wave optical excitation.[22−24] Further, strong spin-exchange interactions between intrinsic excitonic states and embedded Mn spins have a profound effect on QD magneto-optical behaviors. In particular, the alignment of isolated (paramagnetic) Mn spins by an external magnetic field enhances the overall effective magnetic field that is "seen" by band electrons and holes in the host QD. This results in a greatly enhanced, temperature-dependent Zeeman splitting of the QD's electronic states characterized by correspondingly large effective *g*-factors.[4,5,7,25] In turn, the embedded Mn spins can also be aligned by the effective "exchange field" of a QD exciton, which leads to formation of coupled exciton-Mn states known as exciton magnetic polarons.[26−29]

In bulk $Cd_{1-x}Mn_xSe$ alloys and other II−VI diluted magnetic semiconductors (DMS), the magnitude of the effective magnetic field that is seen by electrons and holes in the host material scales with the concentration of Mn ions which behave as isolated (and therefore paramagnetic) spins. At low doping levels (x_{Mn} < 1%), essentially all Mn dopants are isolated and behave paramagnetically (assuming random Mn distribution). However, the effective content of isolated Mn spins ($x_{eff,Mn}$) begins to fall below x_{Mn} at higher doping levels (1% < x_{Mn} < 10%), due to the antiferromagnetic coupling between Mn spins that happen to lie on nearest-neighbor cation sites in the lattice. In fact, the density of isolated Mn spins reaches a maximum value (of about 4%) when x_{Mn} achieves values of about 10−20%,[30,31] beyond which widespread antiferromagnetic coupling within pairs and larger complexes of neighboring Mn spins starts to gradually suppress the paramagnetic response.[30,32] Although doping levels of

Received: August 7, 2020
Published: September 14, 2020

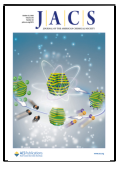

https://dx.doi.org/10.1021/jacs.0c08510
J. Am. Chem. Soc. 2020, 142, 18160−18173

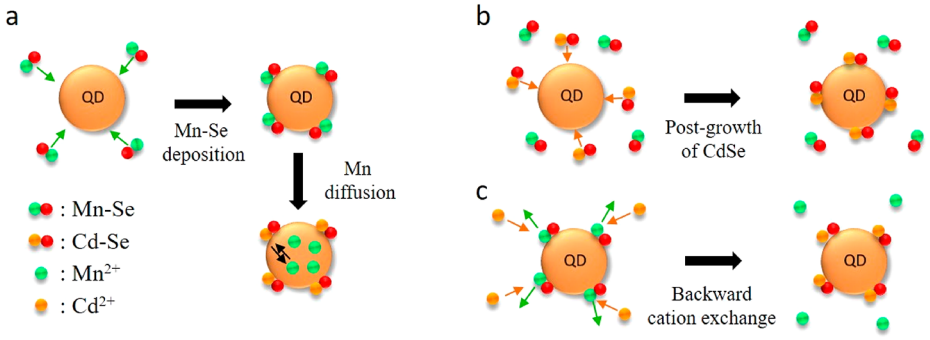

Figure 1. Diffusion doping of CdSe QDs with manganese. (a) Schematic illustration of Mn incorporation into CdSe QDs via diffusion doping. Ideally, incorporation of Mn occurs via addition of Mn−Se units to the surface of the QDs. After initial Mn−Se deposition onto a QD surface, a portion of Mn^{2+} ions diffuses into nanocrystal interior, replacing Cd^{2+} cations. (b) Schematic illustration of the effect of unreacted cadmium on CdSe doping with Mn. The QD doping, via incorporation of the Mn−Se units, competes with uncontrolled (and unwanted) QD postgrowth due to addition of the Cd−Se units. (c) An additional competing process is a backward Mn-for-Cd cation exchange reaction during which Mn^{2+} is replaced with Cd^{2+}.

order 10−20% are fairly modest by the standards of conventional (bulk) II−VI DMS materials, they are difficult to achieve in CdSe QDs, which has been often ascribed to the effect of "self-purification", that is, the expulsion of the dopants to the surface of the QDs.[6,33] Among existing synthetic methods, diffusion doping yields simultaneously high Mn content and good QD size uniformity.[34] This method, however, still exhibits certain deficiencies such as fairly slow reaction rates, increasing size polydispersity in the course of the doping reaction, difficulty in doping of QDs of small sizes, and poor reproducibility.

To address these problems, here we elucidate the factors that control incorporation of Mn into preformed CdSe QDs. We find that one such factor, often overlooked in the previous studies of Mn doping, is the chemistry of original (undoped) CdSe QDs. In particular, we observe that the amount of Mn incorporated into the preformed QDs increases when we decrease the amount of remnant (unreacted) cadmium in the starting CdSe QD sample, which simultaneously results in suppression of widening of size distribution during the doping process. These observations can be rationalized by the fact that in the presence of any remnant Cd-containing species, QD doping via incorporation of the Mn−Se units competes with uncontrolled (and unwanted) QD postgrowth due to addition of the Cd−Se units. After recognizing this problem, we establish a quantitative link between the amount of the remnant cadmium and that of uncontrolled impurities that are present in the synthesis of the original CdSe QDs. We identify these impurities as secondary phosphines and then use this finding to reduce the amount of the unreacted Cd via deliberate introduction of "functional" impurities into the synthesis of CdSe QDs. To further suppress the occurrence of remnant Cd, we apply a postsynthesis treatment of QDs with oleic acid. This helps solubilize the remaining Cd-containing species and then remove them via a standard solvent/nonsolvent purification procedure. The use of controlled amounts of functional impurities during the synthesis of the starting CdSe QDs along with postsynthetic purification allows us to eliminate irreproducibility in the doping procedure and systematically obtain the desired degrees of doping without considerable batch-to-batch variations. Further, this method improves size monodispersity of the resulting doped samples, enhances the rate of Mn incorporation, and allows for achieving very high Mn doping levels that exceed 30% which is confirmed by observations of clear signatures of the onset of the regime where antiferromagnetic Mn−Mn interactions become apparent in the magneto-optical response.

RESULTS AND DISCUSSION

Effects of Uncontrolled Impurities on QD Growth and Incorporation of Mn. For our doping experiments, we prepare wurtzite CdSe QDs following a traditional method, which employs CdO and elemental Se as sources of metal and chalcogen, respectively, in combination with trioctylphosphine (TOP) and trioctylphosphine oxide (TOPO) as a solvent/ligand system[34,35] (see Experimental Section). The QD synthesis can be thought of as comprising four stages (Figure S1a). Stage 1 ("activation of Cd") corresponds to the reaction of Cd with octadecylphosphonic acid (ODPA) which produces $Cd\text{-}ODPA_2$ complexes and also likely OH-Cd-ODPA species.[36,37] It is followed by stage 2 ("preparation for nucleation"), which entails addition of TOP followed by heating. Stages 3 and 4 are, respectively, "nucleation" and "growth" the boundaries between which are not well-defined. The onset of stage 3 is controlled by fast injection of a Se precursor (in our case, TOP-Se) which triggers the formation of Cd−Se-based complexes serving as elementary building blocks of the QDs. In our synthesis, these complexes occur primarily as ODPA-Cd-Se-TOP species.[36,38,39]

For incorporation of manganese into the preformed CdSe QDs, we apply the diffusion doping method of ref 34 wherein the purified wurtzite CdSe QDs are reacted with precursors of Mn and Se whose molar ratio is 1-to-15; the molar amount of Mn is approximately equal to that of Cd in the original (undoped) QDs (see Experimental Section). Ideally, incorporation of Mn occurs via addition of the Mn−Se units to the surface of the QDs which is facilitated by the large excess of Se (Figure 1a). After initial Mn−Se deposition onto a QD surface, a portion of Mn^{2+} ions diffuses into nanocrystal interior, replacing Cd cations.[40] This ideal scenario can be distorted by the presence of uncontrolled amounts of remnant Cd, which can boost an alternative reaction pathway wherein the Se precursor reacts with Cd and then contributes to QD postgrowth via addition of Cd−Se units (Figure 1b). A further complication arises from a backward Mn-for-Cd cation exchange reaction, which is also facilitated by the unreacted Cd species (Figure 1c). These reactions compete with the doping procedure and lead to undesired effects such as a

https://dx.doi.org/10.1021/jacs.0c08510
J. Am. Chem. Soc. 2020, 142, 18160−18173

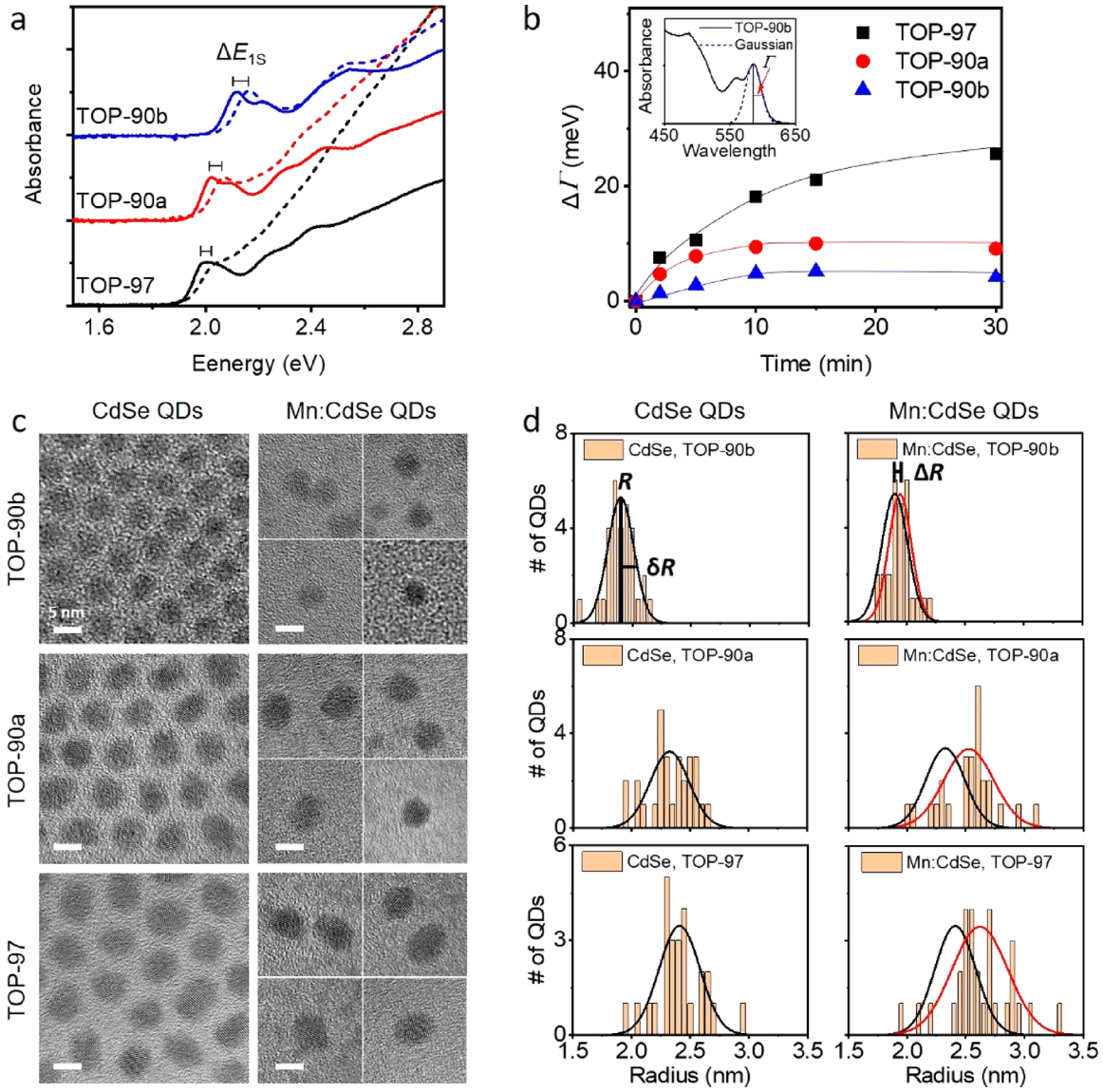

Figure 2. Batch-to-batch inconsistencies in the doping procedure apparent in optical absorption and TEM measurements. (a) Absorption spectra of three CdSe QD samples before (solid lines) and after (dashed lines) incorporation of Mn employing a 10 min doping procedure. The samples were prepared using three different batches of TOP during the synthesis of the original CdSe QDs. In the two batches (samples TOP-90a and TOP-90b), the TOP purity was 90%. In the third batch (sample TOP-97), the TOP purity was 97%. ΔE_{1S} is the 1S peak shift induced by the doping reaction. (b) The difference in the half width at half-maximum (Γ) between the doped and the original undoped sample as a function of the doping reaction time. Inset: Γ was determined by fitting the 1S peak to a Gaussian profile. Solid lines are guides for the eye. (c) TEM images of QD samples TOP-90b, TOP-90a, and TOP-97 before (left column, from top to bottom) and after (right column) incorporation of Mn. Scale bar is 5 nm. (d) Size distributions of QD samples TOP-90b, TOP-90a, and TOP-97 before (left column, from top to bottom) and after (right column) incorporation of Mn. Black and red lines show Gaussian fits of the QD size distribution before and after incorporation of Mn, respectively. R is a QD mean size, δR is a standard deviation of QD sizes, and ΔR is the QD size difference between the doped and the original undoped sample.

reduced rate of Mn incorporation, uncontrolled increase of the mean QD size, and widening of the size distribution. Thus, uncontrolled variation in the amount of Cd-containing species left in the original (undoped) QD sample after the purification procedure may lead to batch-to-batch inconsistencies in the outcome of the doping procedure.

Such inconsistencies are apparent in Figure 2a where we show absorption spectra of three CdSe QD samples before (solid lines) and after (dashed lines) the incorporation of Mn employing a 10 min doping reaction (see Figure S2 for varied times of the doping procedure). These samples were prepared using three different batches of TOP during the synthesis of the original CdSe QDs. In the two batches, the TOP purity was 90%, and in the third, it was 97%. The respective QD samples are labeled as TOP-90a, TOP-90b, and TOP-97.

All three samples show a blue shift of the band-edge (1S) absorption peak following the doping, which is a signature of Mn incorporation into the QD interior and not just deposition of MnSe in the form of an outer shell. The latter process would lead not to a blue shift but rather a red shift of the 1S transition due to the effective increase of the QD size, as typically observed for core/shell structures independent of their type (I, II, or quasi-type II).[41] The blue shift of the 1S exciton, whose energy (E_{1S}) is normally used as a measure of the QD bandgap (E_g), is consistent with the formation of a $Cd_{1-x}Mn_xSe$ alloy. Indeed, the bulk MnSe bandgap (E_g = 2.9 eV at room

https://dx.doi.org/10.1021/jacs.0c08510
J. Am. Chem. Soc. 2020, 142, 18160−18173

temperature[42]) is greater than that of CdSe (E_g = 1.74 eV). For bulk $Cd_{1-x}Mn_xSe$, E_g displays a linear increase with increasing Mn content ($x_{Mn} = x$) with a slope of 1.16 eV/x_{Mn}.[42] In the case of the QDs, the E_{1S} vs x_{Mn} dependence can be more complex due to factors such as the effect of the increasing QD size on the 1S exciton confinement energy and spatial nonuniformity in the distribution of the Mn^{2+} cations. However, the overall trend remains the same, that is, the increase in x_{Mn} leads to the increasing E_g.[34,40]

Although all three QD batches show signatures of successful doping, the TOP-90b sample exhibits a stronger 1S peak blue shift (ΔE_{1S}) than that in the TOP-90a and TOP-97 samples (Figure 2a and Figure S2), suggesting a greater amount of incorporated Mn. Indeed, based on the elemental analysis using inductively coupled plasma atomic emission spectroscopy (ICP-AES), the 10 min doping reaction leads to x_{Mn} = 0.10, 0.071, and 0.079 for the TOP-90b, 90a, and 97 samples, respectively, which corresponds to ΔE_{1S} = 59, 48, and 48 meV. In addition to allowing for a higher level of doping, the use of TOP-90b results in a weaker doping-induced widening of the 1S feature ($\Delta\Gamma$ = 4.8 meV versus 9.4 and 18 meV for the TOP-90a and TOP-97 QDs, respectively), which is a sign of suppressed broadening of the size distribution (Table S1). Here, Γ and $\Delta\Gamma$ are, respectively, the half width at half-maximum (HWHM) of the 1S feature (inset of Figure 2b) and the change in Γ after the doping. Finally, the TOP-90b sample shows a considerably smaller increase in the absorption coefficient (α) at energies above the 1S peak compared to two other samples (Figure 2a). These trends are observed for all durations of the doping procedure (t_d) from 2 to 30 min (Figures 2a and Figure S2).

The above observations indicate that QD doping with manganese proceeds considerably more effectively for the sample prepared with TOP-90b compared to two other batches. To rationalize this result, we hypothesize that in the cases of TOP-90a and 97, the incorporation of Mn via addition of Mn−Se complexes is accompanied by a significant QD postgrowth due to unwanted addition of Cd−Se units (Figure 1b). This would explain the reduced level of doping, the increased QD polydispersity, and the excessive growth of α above E_{1S}.

Direct evidence for strong QD postgrowth and concomitant widening of size dispersion in the case of samples prepared with TOP-90a and 97 is provided by transmission electron microscopy (TEM) measurements (Figure 2c,d). In the ideal scenario, when doping occurs via addition of the Mn−Se units, the relative increase in the QD volume ($\xi_{QD} = \Delta V_{QD}/V_{QD}$; V_{QD} is the mean volume of the original undoped QDs, and ΔV_{QD} is the change in the mean QD volume after the doping) is approximately equal to x_{Mn} (see Supporting Information). In the case of the TOP-90b sample, the doping does seem to occur via this ideal route as ξ_{QD} = 0.07 (top panels of Figure 2c,d) is just slightly less than x_{Mn} = 0.10 determined from the ICP-AES analysis. The situation, however, is different for the TOP-90a and 97 batches for which ξ_{QD} is *ca.* 0.28 (middle and bottom panels of Figure 2c,d, respectively) while x_{Mn} is only 0.07−0.08, that is, a factor of >3 smaller than ξ_{QD}. This is a clear sign of considerable QD postgrowth due to the presence of "unintentional" Cd precursors that apparently were not fully removed from the QD sample during purification. The QD postgrowth is also evident from the strong increase in the QD size polydispersity in the case of the TOP-90a and 97 samples (middle and bottom panels of Figure 2d). We quantify QD size nonuniformity using the ratio of the standard deviation of the QD radii (δR) and the mean QD radius (R): $\chi = \delta R/R$ (Table S2). The TEM measurements indicate that following the doping, χ increases by factors of ∼1.2 and ∼1.3 for the TOP-90a and 97 batches, respectively. On the other hand, χ remains virtually unchanged in the case of the QDs prepared with TOP-90b.

Abundance of Remnant Cd and Doping Efficiency. Since we do not introduce Cd into the doping procedure, its presence in the reaction likely traces back to the original undoped QD sample growth wherein it exists in the form of unreacted Cd precursors and/or Cd−Se complexes. This would further imply that the amount of unreacted Cd-containing species is considerably greater in samples prepared with TOP-90a and 97 compared to that made with TOP-90b.

To validate this conjecture, we quantify the relative fraction of unreacted Cd (f_{Cd}) based on the molar concentrations of Cd in the original CdO precursor (c_{CdO}) and that in the synthesized QD samples (c_{QD}): $f_{Cd} = (c_{CdO} - c_{QD})/c_{CdO} = 1 - c_{QD}/c_{CdO}$. The value of c_{QD} is calculated from $c_{QD} = 10^3 n_{QD}(2V_{QD}/V_0)/N_A$, where n_{QD} is the concentration of the QDs in the final sample (expressed in units of cm^{-3}), V_0 is the volume of the unit cell (factor of 2 before V_{QD}/V_0 accounts for the fact that in CdSe, it contains 2 Cd atoms), and N_A is the Avogadro constant.

To determine the QD concentration, we utilize direct proportionality between n_{QD} and the QD sample absorption coefficient at the peak of the 1S feature: $\alpha_{1S,0} = \gamma\sigma_0 n_{QD}$, where σ_0 is the QD absorption cross-section at the peak of the homogeneous (single-dot) spectral profile and γ is a constant defined by the relationship between the homogeneous 1S absorption line width (Γ_0) and the inhomogeneous (ensemble) broadening of the 1S transition energy due to QD size polydispersity (Γ_{QD}). If $\Gamma_{QD} \ll \Gamma_0$ (size-uniform QD ensemble), γ = 1. When $\Gamma_{QD} \gg \Gamma_0$ (polydisperse QD ensemble), γ can be computed as $\gamma = (\pi \ln 2)^{1/2}(\Gamma_0/\Gamma_{QD})$; see Supporting Information. This leads to the following expression for the QD concentration

$$n_{QD} = (\pi \ln 2)^{-1/2}(\alpha_{1S,0}/\sigma_0)(\Gamma_{QD}/\Gamma_0) \quad (1)$$

In order to determine n_{QD} from eq 1, we substitute α_{1S} and Γ_{QD} with, respectively, the amplitude and the half width of the 1S absorption peak (Figure 2a and inset of Figure 2b). To quantify two remaining parameters (σ_0 and Γ_0), we apply the results of the empirical analysis of CdSe QD absorption spectra of ref 43 (see Experimental Section).

Using the above approach, we find that in the undoped samples prepared with TOP-90a and TOP-97, f_{Cd} is, respectively, 50% and 61% (Table S3). Both of these values are considerably larger than that for the sample synthesized using TOP-90b for which f_{Cd} = 28%. These findings point toward the direct link between the amount of remnant Cd and the propensity of QDs to uncontrolled postgrowth during the doping procedure.

Next, we aim to elucidate an underlying reason for a considerable difference in f_{Cd} between the studied samples. Since all three QD batches were prepared using nominally identical reaction conditions, the difference in Cd consumption during the synthesis should probably be ascribed to the presence of "functional" impurities in the reactants. In our evaluation of the influence of such impurities, we paid special attention to phosphine species that were previously observed

https://dx.doi.org/10.1021/jacs.0c08510
J. Am. Chem. Soc. 2020, 142, 18160−18173

to have a strong effect on QD synthesis.[38,39,44−47] In particular, several literature studies demonstrated that the presence of these impurities in TOP and TOPO could dramatically modify the kinetics of CdSe QD growth, leading to considerable batch-to-batch variations in QD sizes, shapes, and size/shape uniformity even in the case of reactants of nominally identical purity.[44,45]

To detect the presence of potentially important impurities, we conduct a compositional analysis of three batches of TOP employed in the synthesis of QD samples shown in Figure 2a using a ^{31}P nuclear magnetic resonance (NMR) spectroscopy. We observe that in all three cases, the NMR spectra are dominated by the TOP peak at −32 ppm,[39,46] which we use as a reference in our comparison of NMR features between the studied QD samples (Figure 3a). In particular, if the spectra are normalized so as to match the amplitude of the TOP peak, the TOP-90b sample shows an additional prominent peak at −69 ppm, which is much more intense compared to a similar peak in the spectra of the two other samples. This feature can be ascribed to the secondary phosphine, dioctylphosphine (DOP), which is a typical impurity found in moderate purity TOP.[39,46] On the basis of the NMR spectrum of the TOP-90b sample, the molar amount of DOP is ∼1% of pure TOP, and it drops to 0.04% and 0.03% in the TOP-90a and 97 samples, respectively.

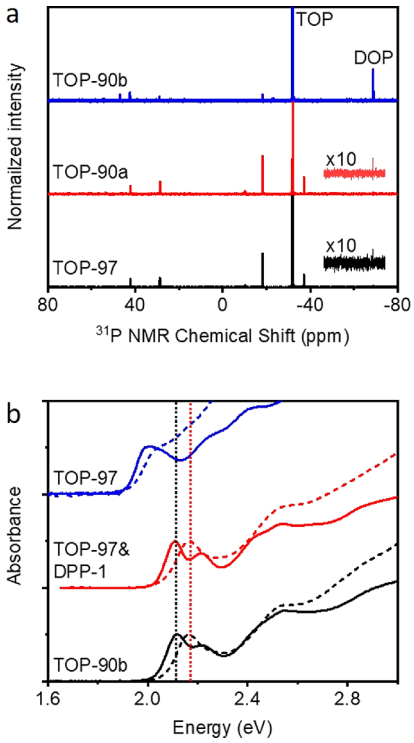

Figure 3. Correlations between the abundance of DOP impurities and the efficiency of doping revealed by NMR and optical absorption spectroscopies. (a) ^{31}P NMR spectra of TOP from three different batches, TOP-90b (top), TOP-90a (middle), and TOP-97 (bottom), normalized by the amplitude of the TOP NMR peak at −32 ppm. The DOP peak appears at −69 ppm. (b) Absorption spectra of three CdSe QD samples before (solid lines) and after (dashed lines) incorporation of Mn employing a 10 min doping procedure. The spectra at the top (blue) and the bottom (black) correspond to QD samples synthesized using TOP of 97% or 90% (batch TOP-90b) purity, respectively. The spectra in the middle correspond to the QDs prepared using TOP-97 with a 1% addition of DPP (molar fraction relative to TOP). The two vertical dashed lines highlight that the absolute positions and the doping-induced blue shifts of the 1S peak are nearly the same for the QDs synthesized using TOP-90b and a mixture of TOP-97 and DPP.

Another intense NMR peak is at −18 ppm. On the basis of its position, it can be assigned to the branched-chain TOP isomer, 1-methylheptyl-di-*n*-octylphosphine.[45] The presence of this isomer, however, is not expected to affect the QD synthesis because it features the same type of the phosphine functional group as TOP and, therefore, it does not introduce any new chemical behaviors into the growth reaction. As was observed previously,[39,47,48] the DOP impurities can dramatically modify the kinetics of QD growth. In particular, in the case of the synthesis employed in the present work, DOP can influence the growth reaction by replacing ODPA in the Cd-ODPA$_2$ complexes, which will result in the formation of Cd-DOP$_2$ and possibly ODPA-Cd-DOP species. These species are more reactive than the original Cd-ODPA$_2$ precursor because of the stronger Lewis acidity of their Cd^{2+} cations.[45] This should enhance the rate of consumption of Cd and thereby reduce its abundance in the reaction products at the completion of the QD synthesis.

Control of Remnant Cd with "Functional" Impurities. A known effect of the increased reactivity of Cd precursors is the enhanced rate of QD nucleation.[39,46−48] The fact that the undoped QD sample prepared with TOP-90b exhibits a bluer 1S absorption peak than the two other samples (Figure 2a) suggests that such enhancement is indeed realized in our experiments. The higher energy of the 1S peak indicates a smaller mean size of the final QDs. This is typically a sign of faster nucleation, which produces a larger number of QD seeds and, as a result, leaves a smaller amount of precursors for follow-up QD growth.

To verify the feasibility of the above scenario and, in particular, confirm strong influence of DOP impurities on kinetics of QD growth, we modify stage 2 of our synthesis by adding to higher purity TOP (97%) varied amounts of secondary phosphines (Figure S1b). Instead of DOP, we use commercially available diphenylphsosphine (DPP). The DPP molecules feature the same type of the H−P bond as DOP; therefore, they are expected to behave similarly with DOP in reactions where H is replaced by Cd. In our synthesis, this reaction occurs during stage 2 when it generates Cd-DPP$_2$ species from the Cd-ODPA$_2$ complexes.[47,48]

First, we verify that the effect of DPP is similar to that of DOP. To imitate the conditions realized during the synthesis with TOP-90b when [DOP]:[TOP] = 1:100 (Figure 3a), we add p_{DPP} = 1% of DPP to TOP of the 97% purity. The addition of DPP leads to the expected effect of faster nucleation and correspondingly smaller QDs as indicated by a blue shift of the 1S absorption feature compared to the sample synthesized with pure TOP-97 (red and blue solid lines in Figure 3b, respectively). The 1S peak position of the sample prepared with DPP is virtually identical to that in the undoped TOP-90b sample (compare red and black lines in Figure 3b). We also observe close similarities between absorption spectra of these two samples following the doping procedure (dashed red and black lines in Figure 3b). These results indicate that the "functional" effect of DPP during the QD synthesis is similar to that of DOP.

Next, we demonstrate that using DPP we can systematically control the rate of QD nucleation by varying p_{DPP}. In Figure 4a, we display the absorption spectra of four CdSe QD samples

https://dx.doi.org/10.1021/jacs.0c08510
J. Am. Chem. Soc. 2020, 142, 18160−18173

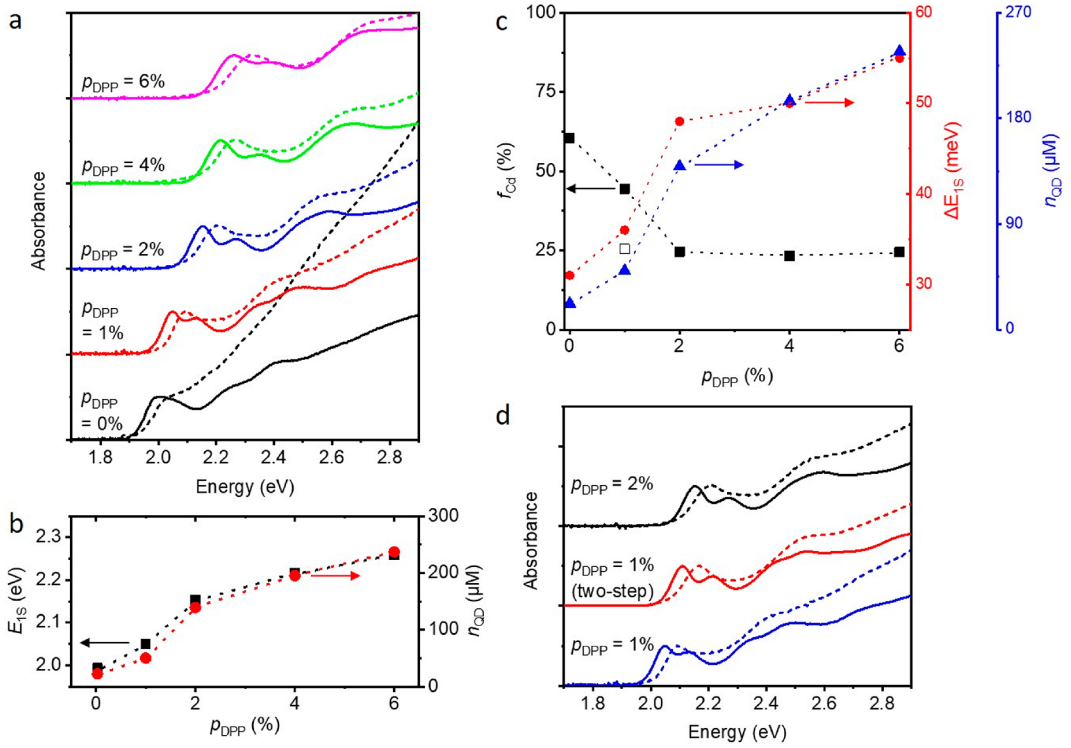

Figure 4. Effect of controlled amounts of "functional" DPP impurities on the efficiency of doping. (a) Absorption spectra of CdSe QD samples synthesized using TOP-97 with the addition of DPP (introduced during stage 2 of the synthesis) in the amount p_{DPP} = 1, 2, 4, and 6% (colored lines) in comparison to the QDs synthesized without DPP (p_{DPP} = 0; black lines) before (solid lines) and after (dashed lines) incorporation of Mn employing a 10 min doping procedure. (b) The 1S peak position (black squares) and the QD concentration (red circles) for the original (undoped) QDs as a function of the amount of DPP (p_{DPP}); same samples as in 'a'. Dotted lines are guides for the eye. (c) The fraction of remnant Cd (black solid squares) and the QD concentration (blue solid triangles) in the original QD sample and the 1S peak blue shift induced by incorporation of Mn (red solid circles) as a function of the amount of DPP used in the synthesis of the QDs; same samples as in 'a'. Dotted lines are guides for the eye. The black open square shows f_{Cd} for the QDs prepared using a two-step addition of DPP (1% at stage 2 and 1% at stage 3). Dotted lines are guides for the eye. (d) Absorption spectra of CdSe QDs prepared using a single-step addition of DPP with p_{DPP} = 1% (blue) and 2% (black) along the spectra of the sample synthesized with a two-step addition of DPP (1% at each step; red) before (solid lines) and after (dashed lines) doping (t_d = 10 min).

prepared using p_{DPP} = 1, 2, 4, and 6% (colored line) in comparison to the QDs synthesized without DPP (p_{DPP} = 0; black lines); the solid and dashed lines correspond to samples before and after doping, respectively. For all samples made with DPP, 1S peak is blue-shifted compared to that prepared without DPP and the observed shift progressively increases with p_{DPP}, indicating the decrease in the QD size, which suggests the increase in the rate of QD nucleation. Indeed, the evaluation of the QD concentration in the synthesized samples indicates that n_{QD} progressively increases with increasing p_{DPP} (Table S4), which occurs in direct correlation with the 1S feature blue shift (Figure 4b). These results point toward a strong effect of DPP on the rate of QD nucleation which can be exploited for controlling the amount of remnant Cd.

To prove that the acceleration of QD nucleation caused by the increasing amount of DPP leads to improved consumption of Cd, we use the measurements of Figure 4a,b to quantify the relative amount of unreacted Cd (f_{Cd}). In Figure 4c, we plot f_{Cd} together with n_{QD} as a function of p_{DPP}. This plot reveals a close correlation between the increase in n_{QD} and the decrease in f_{Cd}, both of which are controlled by the amount of DPP. In particular, in the case of pure TOP-97 (p_{DPP} = 0), the fraction of remnant Cd is ~61% of the original amount of the Cd precursor. f_{Cd} decreases to ~44% for p_{DPP} = 1% and, then, to ~25% for p_{DPP} of 2% or more. Importantly, the drop in the amount of unreacted Cd due to increasing p_{DPP} is accompanied by the increase in the postdoping shift of the 1S peak (ΔE_{1S}) indicating a more effective incorporation of Mn. Simultaneously, we observe the suppression of the QD postgrowth manifested as a reduction in the deviation of the higher-spectral-energy part of the absorption spectrum of the doped sample from that of the original undoped QDs (Figure 4a).

In the above synthetic scheme, the introduction of the increasing amount of DPP leads to the reduction in the size of the product QDs. In some situations, however, it desirable to lessen the effect of DPP on the QD size but at the same time enable effective doping by limiting the amount of remnant Cd. In order to accomplish this objective, we have modified the QD growth reaction by reducing the amount of DPP added during stage 2 to a "suboptimal" value (in our experiments, 1% versus TOP) and simultaneously adding more DPP (typically, also 1% versus TOP) together with TOP-Se at stage 3 (Figure S1b). The purpose of this two-step DPP addition scheme is to limit the rate of nucleation (stage 3) but at the same time enhance Cd consumption in the course of QD growth (stage 4).

The results of this approach are illustrated in Figure 4d, which shows the absorption spectra of the undoped (solid lines) and doped (dashed line) CdSe QDs prepared using a two-step DPP addition (1% versus TOP at each step; red) in comparison to those for the single-step addition scheme with 1% (blue) and 2% (black) of DPP. On the basis of the

https://dx.doi.org/10.1021/jacs.0c08510
J. Am. Chem. Soc. 2020, 142, 18160−18173

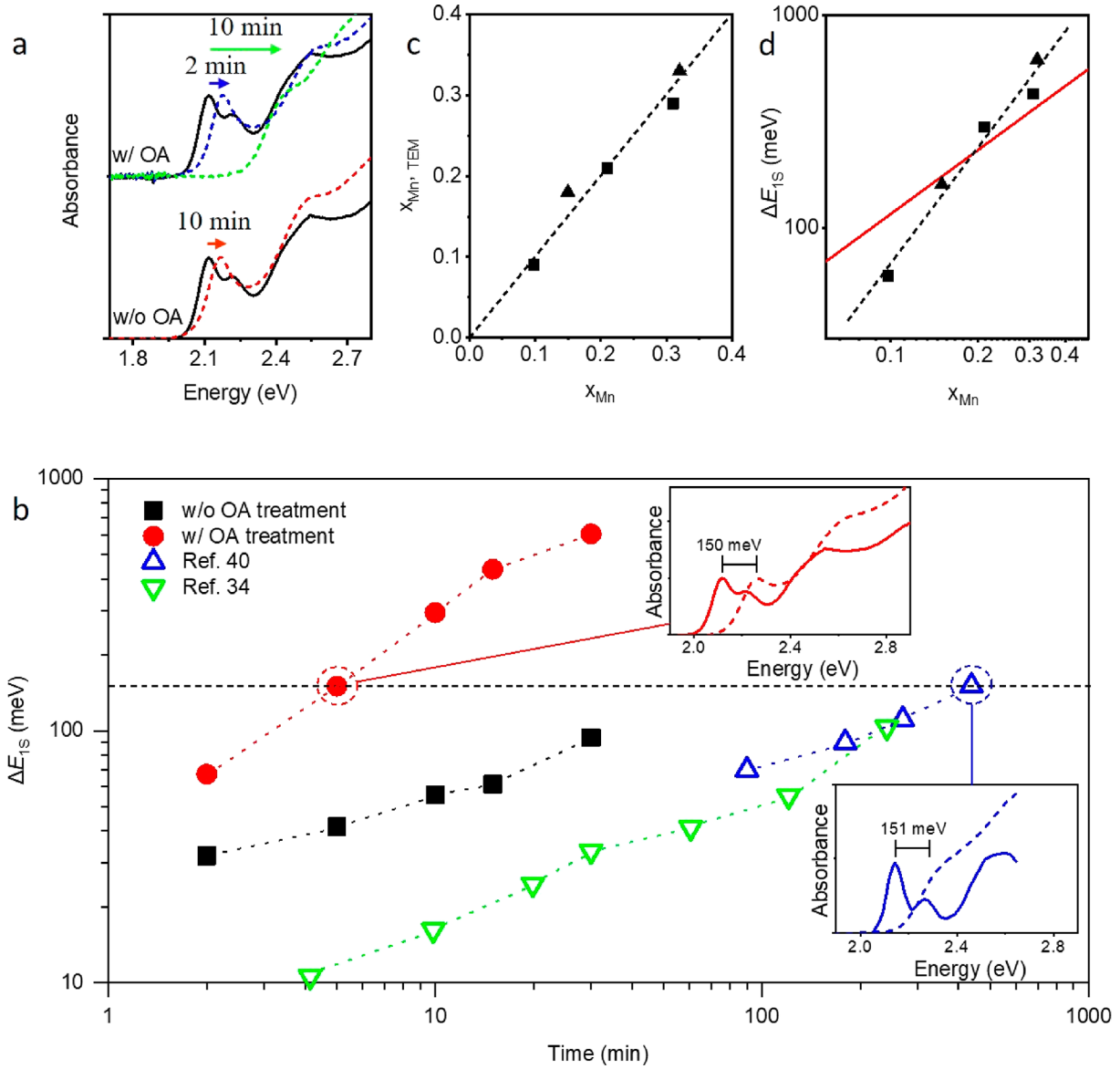

Figure 5. Quantification of Mn contents and doping dynamics. (a) Absorption spectra of the CdSe QDs purified without (bottom) and with (top) OA before (solid lines) and after (dashed lines) doping (t_d = 2 and 10 min). The OA treatment was applied before the doping procedure. (b) The doping induced 1S peak blue shift for the QD samples purified with (red solid circles) and without (black solid squares) OA treatment as a function of duration of the doping procedure. Open triangles are literature data from refs 34 (green) and 40 (blue). The inset at top (red lines) are absorption spectra of the CdSe QDs before (solid) and after (dashed) incorporation of Mn (t_d = 5 min, present study). The inset at bottom (blue lines) are the same type of spectra from ref 40 for the 7.3-h doping reaction. In the case of the doped samples with a poorly defined 1S absorption feature (as, *e.g.*, in the bottom inset), the band-edge position was inferred from the minimum of the 2nd derivative of the absorption spectrum. (c) A close correspondence between the Mn content obtained from the ICP-AES measurements (x_{Mn}) and that estimated from the TEM measurements of the QD volume expansion ($x_{Mn,TEM}$) indicates that doping proceeds according to a nearly ideal scenario, that is, it occurs by addition of the Mn−Se units without a competing processes of surface deposition of the Cd−Se species. The triangles are the data for the CdSe QDs prepared using a two-step addition of DPP (1% of the TOP molar amount at each step), and the squares are the data for the samples prepared using TOP-90b without the DPP addition. In the latter case, Mn incorporation is facilitated by the presence of secondary phosphines occurring as DOP impurities (~1% of the molar amount of TOP). (d) The doping-induced shift of the 1S feature as a function of the average per-dot Mn content (x_{Mn}) obtained from the ICP-AES measurements (symbols; same samples as in panel 'c'). The observed dependence shows a nearly quadratic behavior, $\Delta E_{1S} \propto (x_{Mn})^m$, with the log−log slope m = 1.8. The red line is the bandgap of bulk $Cd_{1-x}Mn_xSe$ which shows a linear dependence on x_{Mn} (m = 1).

positions of the 1S band-edge peak, the two-step approach leads to larger QDs compared to those produced with a single-step method for p_{DPP} = 2%. Simultaneously, it results in the improved consumption of Cd compared to the single-step approach with 1% of DPP. In fact, the amount of remnant Cd in this case (f_{Cd} = 26%; open square in Figure 4c) is reduced to nearly the same level as for the single-step DPP addition with $p_{DPP} \geq 2\%$ (f_{Cd} is ~25%). Importantly, the two-step scheme also leads to a comparable amount of incorporated Mn, as indicated by a similar value of the doping-induced 1S peak blue shift (~60 meV in both cases). All of these findings confirm our original conjecture that the effectiveness of CdSe QD doping with Mn strongly depends on the amount of remnant cadmium in the undoped sample and, further, that

https://dx.doi.org/10.1021/jacs.0c08510
J. Am. Chem. Soc. 2020, 142, 18160−18173

this amount can be controlled by introducing "functional" impurities into the QD synthesis for accelerating the consumption of Cd precursors either at the stage of QD nucleation or both nucleation and follow-up growth.

QD Purification. As indicated by data of Figure 4c (black squares), while leading to a considerable reduction of f_{Cd}, the addition of secondary phosphines does not completely eliminate remnant Cd, whose fraction saturates at the *ca.* 25% level of the Cd amount originally introduced into the reaction. This incomplete consumption of the Cd precursor is likely due to the presence of weakly reactive OH-Cd-ODPA species created at the stage of "Cd activation" together with more chemically active Cd-ODPA$_2$ species.[49,50] Due to their limited solubility in either polar or nonpolar solvents, the OH-Cd-ODPA complexes are difficult to remove from the QD sample via a standard purification method, which employs repeating cycles of QD precipitation with a polar solvent (typically, ethanol) followed by redispersion in a nonpolar solvent (typically, toluene). In order to resolve the problem of poor solubility of the OH-Cd-ODPA species, we modify the purification procedure by adding an additional step of treatment with oleic acid (OA) which leads to the replacement of hydroxyl groups with oleate (OL) groups (see Experimental Section and Figure S3). The resulting OL-Cd-ODPA complexes are soluble in nonpolar solvents, and, therefore, can be removed from the QD sample by a standard solvent/nonsolvent treatment (see Experimental Section and Figure S3).

The use of the modified purification scheme allows us to greatly improve the incorporation of Mn into the QDs. For example, the 10 min doping procedure applied to a QD sample, which has not undergone the OA treatment, leads to a 56-meV shift of the 1S peak (Figure 5a, two spectra at the bottom). In the case of the OA-treated QDs, a 2 min doping reaction produces the 67-meV shift (black and blue spectra in Figure 5a). If the reaction time is extended to 10 min, the shift becomes as large as 294 meV (green spectrum in Figure 5a). A further increase in the duration of the doping procedure leads to the gradual saturation of ΔE_{1S} (Figure 5b, red circles). For the longest reaction time used in our experiments (30 min), the 1S shift reaches 604 meV, which corresponds to x_{Mn} of ~32% based on the ICP-AES measurements (Figure 5b,c and Figure S4). As we show later in this work, this level of doping is well above the critical value for the onset of antiferromagnetic effects.

Doping Dynamics and Underlying Mechanism. It is illustrative to benchmark the kinetics of the doping reaction realized in the present study against those from the published literature reports that explored diffusion doping.[34,40] For this purpose, we compare the ΔE_{1S} vs t_d dependence for our doped samples (solid symbols in Figure 5b) with that for the samples from refs 34 and 40 (open triangles). It is apparent that the revised doping method of the present study leads to a much faster incorporation of Mn which translates into considerably higher doping levels for the same reaction time. For example, in the case of t_d = 30 min, the doping procedure of ref 34 yields ΔE_{1S} = 33 meV, while our doping method results in ΔE_{1S} = 94 meV for the sample prepared without OA purification and 604 meV for the OA-treated sample. The studies of ref 40 showed that it was possible to push ΔE_{1S} to 151 meV; however, this required a t_d of >7.30 h (Figure 5b). Using our doping procedure, we can achieve a comparable value of ΔE_{1S} with t_d of only 5 min. Importantly, the new method also leads to a sharper band-edge absorption feature in the doped samples (compare top and bottom insets of Figure 5b) indicating a tighter QD size dispersion.

The high per-dot contents of Mn observed in our samples suggest that the developed synthetic approach leads to a nearly ideal regime of diffusion doping when incorporation of Mn occurs exclusively via addition of Mn−Se units without QD postgrowth due to deposition of Cd−Se complexes. To confirm this conjecture, we apply TEM measurements to analyze the QD mean sizes before and after doping and, then, calculate the level of doping ($x_{Mn,TEM}$) assuming that the size increase occurs entirely due to the added Mn−Se species (see Supporting Information). The results of this analysis are displayed in Figure 5c, where we plot $x_{Mn,TEM}$ as a function of x_{Mn} determined from the elemental analysis. The plotted data exhibit a nearly perfect linear dependence ($x_{Mn,TEM} \approx x_{Mn}$) indicating that our doping scheme leads to the complete suppression of unwanted QD postgrowth and thereby allows for highly efficient incorporation of Mn.

The conducted measurements also allow us to obtain a quantitative relationship between the change in the QD bandgap (ΔE_g) determined from the shift of the 1S absorption feature ($\Delta E_g = \Delta E_{1S}$) and the average content of incorporated Mn (symbols in Figure 5d). As we mentioned earlier, in a bulk $Cd_{1-x}Mn_xSe$ alloy, ΔE_g depends linearly on x_{Mn} (red line in Figure 5d). In the case of our doped QD samples, however, the dependence of ΔE_{1S} *versus* x_{Mn} is nearly quadratic as indicated by the log−log slope (m) of 1.8 (black dashed line in Figure 5d). The amplified sensitivity of the bandgap to changes in x_{Mn}, in this case, is due to the additional contribution from the effect of quantum confinement. As we discussed earlier, in the diffusion doping method, the Mn content decreases from the periphery of the dot toward its center, which leads to a radially modulated confinement potential created by the compositionally graded $Cd_{1-x}Mn_xSe$ alloy layer. The increase in the thickness of this layer with increasing average Mn content results in a progressive "squeezing" of the electronic wave functions within the QD central volume, which increases the effective bandgap and accelerates its dependence on x_{Mn} compared to bulk alloys. A further consequence of this effect is that the magneto-optical properties of the QD will be especially sensitive to the details of the nonuniform doping profile, particularly toward the center of the QD where the electronic wave functions have maximum amplitude.

Magneto-Optical Properties of Doped QDs. The incorporation of magnetic Mn ions (spin S = 5/2) into II−VI semiconductor QDs leads to enhanced magneto-optical properties typical of DMS materials.[1−10] These properties arise from strong sp-d exchange interactions between QD excitons and magnetic spins of Mn impurities. One manifestation of these interactions is a large enhancement of the Zeeman splitting of the QD electronic states by the applied magnetic field (B) which leads to "giant" effective exciton g-factors (g_{eff}).[4,5,7,25] This phenomenon can be ascribed to the effect of field-aligned Mn spins which lead to the increase in the effective magnetic field acting on a QD exciton.

The sp-d spin-exchange interactions have "contact" nature, that is, they originate from the interaction between the QD's electron and hole wave functions (which have s- and p-type Bloch components, respectively) and the d-type wave functions of the electrons that comprise the spin-5/2 Mn ion. Crucially, these interactions depend on the overlap of the carrier envelope wave functions, $\Psi_e(r_e)$ and $\Psi_h(r_h)$, with the

https://dx.doi.org/10.1021/jacs.0c08510
J. Am. Chem. Soc. 2020, 142, 18160−18173

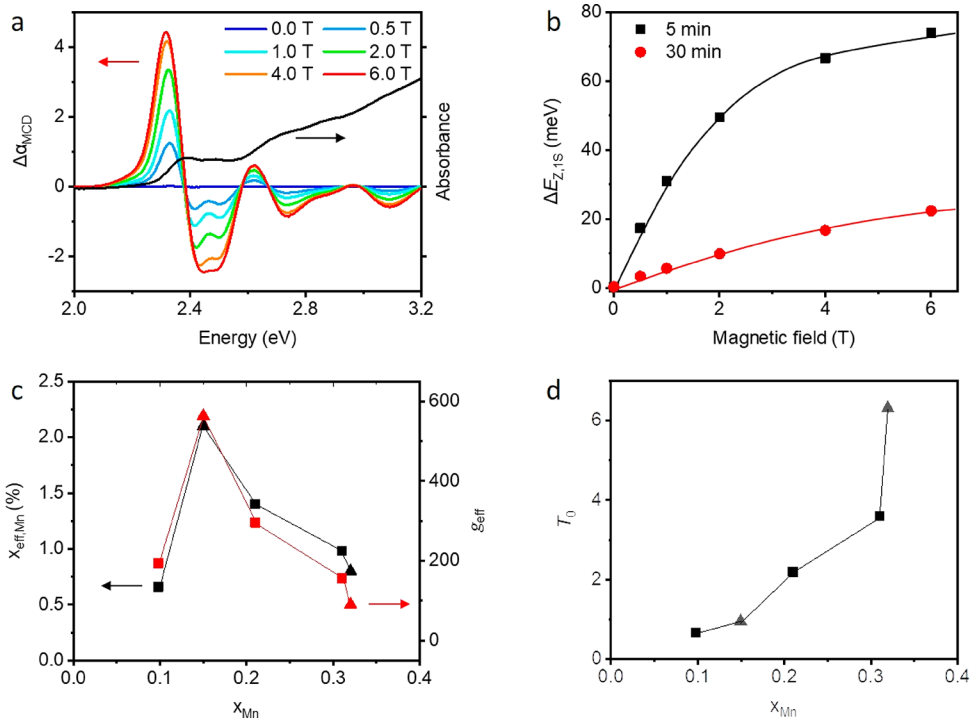

Figure 6. Magneto-optical measurements of Mn-doped QDs. (a) Absorption (black line) and *B*-dependent MCD spectra of Mn-doped CdSe QDs (colored lines) prepared using t_d = 5 min (x_{Mn} = 0.15). The original (undoped) QDs were synthesized using a two-step addition of DPP (1% at each step). (b) The Zeeman splitting of the band-edge 1S transition of the Mn-doped CdSe QDs prepared using t_d = 5 min (x_{Mn} = 0.15, black squares) and 30 min (x_{Mn} = 0.32, red circles) as a function of magnetic field. The solid lines are fits using a modified Brillouin function. On the basis of these fits, the effective Mn contents in these two samples are $x_{eff,Mn}$ = 2.1% and 0.8%, respectively. The drop in $x_{eff,Mn}$ for the sample with a higher total Mn content is due to formation of antiferromagnetically bound Mn complexes. (c) The plots of $x_{eff,Mn}$ (black symbols) and the effective *g*-factor (red symbols) obtained from the MCD spectra (panel 'a' and Figures S5 and S6) versus the average per-dot Mn content. As in Figure 5c,d, triangles and squares correspond to Mn-doped samples prepared using starting QDs synthesized with, respectively, TOP-90b and a combination of TOP-97 and DPP. (d) The effective temperature (T_0) versus average Mn content (x_{Mn}); same samples as in panel 'c'.

Mn ions, and are therefore most pronounced when magnetic impurities are incorporated deep into the QD *interior*, where $\Psi_{e,h}(r_{e,h})$ has a large amplitude. Mn ions on the QD surface contribute very little to the net sp-d exchange, because $\Psi_{e,h}(r_{e,h})$ approaches zero at the QD surface. In the case of diffusion doping, a considerable number of Mn ions are located in the QD near-surface area. Therefore, the content of magnetic impurities that overlap significantly with $\Psi_{e,h}(r_{e,h})$ and lead to enhanced magneto-optical properties is usually much lower than the overall Mn content derived from the elemental analysis (x_{Mn}). Moreover, as discussed above, antiferromagnetic coupling between nearest-neighbor Mn cations further suppresses the number of isolated paramagnetic spins, an effect that becomes quite significant for Mn contents exceeding 10−20%. With increasing level of Mn doping, a maximum in the enhanced paramagnetic response is therefore expected, similar to the well-studied case of conventional bulk DMS materials. For even higher Mn doping levels, we anticipate a reduction of the paramagnetic response, together with additional hallmark signatures of widespread antiferromagnetic Mn coupling.[51]

To evaluate the accessible range of Mn doping using our method, and in particular to determine whether we can achieve the regime of the maximum paramagnetic response and even beyond (where antiferromagnetic coupling "turns on"), we study magneto-optical properties of the synthesized $Cd_{1-x}Mn_xSe$ QDs using magnetic circular dichroism (MCD) spectroscopy at low temperatures (T = 2.75 K) and in applied magnetic fields B up to 6 T. An MCD experiment detects the difference between the sample's absorption coefficient ($\Delta\alpha_{MCD}$) for right- and left-circularly polarized light from which the exciton's Zeeman splitting can be inferred (see Experimental Section).

Figure 6a shows an example of *B*-dependent MCD spectra for the Mn:CdSe QD sample prepared using a 5 min doping reaction for which elemental analysis yields an overall doping level x_{Mn} = 15%. The MCD spectra comprise a series of overlapping "dispersive" features that correspond to discrete optical transitions of the QDs. By analyzing the band-edge part of the MCD spectra, we obtain the Zeeman splitting of the lowest-energy 1S transition ($\Delta E_{Z,1S}$). Figure 6b shows $\Delta E_{Z,1S}$ obtained from this analysis as a function of B for samples prepared using t_d = 5 min (black squares) and 30 min (red circles). The initial linear growth of $\Delta E_{Z,1S}$ is followed by saturation, which corresponds to the regime when all the isolated (paramagnetic) Mn spins are aligned by the field. That is, $\Delta E_{Z,1S}$ follows the field-dependent magnetization of the "free" Mn spins that reside within the electron and hole envelope wave functions $\Psi_{e,h}(r_{e,h})$. Following standard analyses of conventional DMS materials,[34,52] $\Delta E_{Z,1S}$ can be expressed as

$$\Delta E_{Z,1S} = g_{int}\mu_B B + N_0(\alpha - \beta)x_{eff,Mn} < S_Z > \quad (2)$$

where

$$< S_Z > = SB_S[g_{Mn}\mu_B SB/k_B(T + T_0)] \quad (3)$$

https://dx.doi.org/10.1021/jacs.0c08510
J. Am. Chem. Soc. 2020, 142, 18160−18173

The first term on the right-hand side of eq 2 is the intrinsic Zeeman splitting of the exciton in the QD host, which is small, temperature-independent, and scales linearly with B. It is proportional to the product of μ_B (the Bohr magneton) and the intrinsic exciton g-factor (g_{int}) which in CdSe QDs is close to +1.[53,54] The second term in eq 2 describes the additional contribution arising from the sp-d exchange interactions between the QD exciton and the Mn spins, where $N_0\alpha$ and $N_0\beta$ are the s-d (conduction band) and p-d (valence band) exchange constants. The parameter $x_{eff,Mn}$ is the effective concentration of free (paramagnetic) Mn spins that are "seen" by the exciton. This quantity depends on the Mn density profile in the QD, $\rho_{Mn}(r)$ and its overlap with the carrier wave functions. Finally, $<S_Z>$ is the average projection of the Mn spins along the applied field B. Due to competition between field-induced spin alignment and thermal disordering, $<S_Z>$ is temperature- and field-dependent and can be described by the modified Brillouin function B_S, where k_B is the Boltzmann constant, g_{Mn} is the Mn g-factor, and T_0 is an effective temperature that accounts for antiferromagnetic coupling between Mn spins.[32,52]

Two key concepts are contained in these equations. First, the maximum (saturated) Zeeman splitting depends on $x_{eff,Mn}$ which is typically less than the actual Mn content (x_{Mn}) owing to details of the spatial overlap of $\rho_{Mn}(r)$ with $\Psi_e(r_e)$ and $\Psi_h(r_h)$, and due to antiferromagnetic coupling between neighboring Mn cations. This difference becomes increasingly significant at higher Mn doping levels where the probability of neighboring Mn increases. In bulk DMS crystals where $\rho_{Mn}(r)$ is uniform, $x_{eff,Mn}$ can be as large as ~4% when x_{Mn} is around 10−20%, beyond which it falls for even larger x_{Mn}. Second, the effective temperature T_0 provides a reliable indicator of antiferromagnetic coupling between Mn spins and therefore of the local Mn concentration. From early studies of heavily Mn-doped II−VI crystals, it was found that the measured magnetization (and the corresponding exciton Zeeman splitting) saturated more slowly with applied field than predicted as if the temperature were larger than the actual experimental temperature by an amount T_0. This phenomenon originates in the antiferromagnetic coupling between Mn spins and is captured very well by the inclusion of T_0. Crucially, T_0 increases rapidly at high Mn contents where x_{Mn} > 20% thereby providing an independent confirmation of heavy Mn doping.

To determine an effective content of isolated internally located Mn spins in our doped QD samples, we fit the measured $\Delta E_{Z,1S}$ vs B dependence to eq 2 using $x_{eff,Mn}$ as an adjustable parameter and assuming that the exchange constants are equal to those of bulk $Cd_{1-x}Mn_xSe$ ($N_0\alpha$ = 0.23 eV and $N_0\beta$ = −1.27 eV). Applying this analysis to the t_d = 5 min sample (black squares in Figure 6b), we obtain $x_{eff,Mn}$ = 2.1%. This value is considerably lower than the total Mn content obtained from the elemental analysis (x_{Mn} = 15%). As we discussed earlier, this is the expected outcome of the diffusion doping method for which only a small fraction of the total number of dopants (~14% in our case) is incorporated into the dot interior, while the majority of them resides near the QD surface. In the present example, the average overall per-dot number of Mn ions is 90, while the number of internal dopants is only 13.

When we apply a similar analysis to the sample prepared using t_d = 30 min (red circles in Figure 6b), we obtain $x_{eff,Mn}$ = 0.8%. Despite a higher total Mn content (x_{Mn} = 32%) compared to the 5 min sample, the corresponding value of $x_{eff,Mn}$ is noticeably lower. This suggests that the amount of internally incorporated Mn ions in this case becomes so high that newly added Mn ions combine with previously incorporated dopants to create antiferromagnetically coupled Mn complexes, which reduces the content of magneto-optically active isolated Mn spins.

The signatures of high Mn doping levels realized in our QDs are evident from plots of $x_{eff,Mn}$ vs x_{Mn} (Figure 6c) and T_0 vs x_{Mn} (Figure 6d). In particular, Figure 6c shows a clear peak in the plot of $x_{eff,Mn}$ vs x_{Mn}, which occurs for x_{Mn} = 15%. QDs with higher x_{Mn} show significantly smaller Zeeman splitting indicating the reduced $x_{eff,Mn}$. In strong support of this picture, Figure 6d shows that the measured T_0 is small (<1 K) when x_{Mn} is low but grows significantly (T_0 > 6 K) when x_{Mn} is large, again indicating strong antiferromagnetic coupling of the spins in the QD. From early studies of bulk DMS crystals, T_0 > 6 K is typically associated with Mn concentrations exceeding 30%, in good agreement with our elemental analyses of the most heavily doped QDs.

Interestingly, the peak value of $x_{eff,Mn}$ realized in our QD samples is lower than that in bulk $Cd_{1-x}Mn_xSe$ alloys by a factor of 2 (2.1% vs 4.2%). To understand this difference it is important to keep in mind that in the QDs, $\rho_{Mn}(r)$ is not radially uniform and that $x_{eff,Mn}$ represents a spatial average which accounts for both the nonuniformity of the distribution of Mn ions within the QD as well as the details of the spatial distribution of electron and hole wave functions. In particular, the wave functions and $\rho_{Mn}(r)$ have opposite radial dependences; *i.e.*, the envelope wave functions are maximal at the center of the QD where $\rho_{Mn}(r)$ is smallest but approach zero at the QD periphery where $\rho_{Mn}(r)$ is largest. As a result, the number of Mn spins strongly interacting with the QD exciton is lower compared to the case of a spatially uniform distribution of magnetic impurities even if the overall per-dot Mn content is the same.

The conducted MCD measurements also allow us to estimate effective excitonic g-factors of the doped QD samples. For this purpose, we use expression $g_{eff} = \Delta E_{Z,1S}/(\mu_B B)$ applied to a linear part of the measured $\Delta E_{Z,1S}$ vs B dependence (Figure 6b). The results of these estimations are displayed in Figure 6c (red symbols) together with the data for $x_{eff,Mn}$ discussed earlier (black symbols). As expected, both quantities exhibit similar overall dependences on average content of Mn impurities. In particular, when x_{Mn} is increased, g_{eff} first also increases and, then, starts to decrease due to the onset of antiferromagnetic interactions between closely located Mn spins. The effective g-factor peaks at x_{Mn} of 15% at which point it reaches an extremely high value of ~600 (see Table S5 for the summary of the present magneto-optical measurements and the comparison with literature results). This once again confirms very efficient incorporation of Mn ions into the QDs enabled by the developed doping method.

CONCLUSION

We conducted a comprehensive study of diffusion doping of CdSe QDs with manganese impurities. Specifically, we focused on three problems: inconsistencies in the outcome of the existing doping procedures manifested in large batch-to-batch variations in the resulting Mn content; a considerable broadening of QD size dispersion often observed after the doping; and the difficulty in obtaining high Mn doping levels required for maximizing $x_{eff,Mn}$. We show that all of these

https://dx.doi.org/10.1021/jacs.0c08510
J. Am. Chem. Soc. 2020, 142, 18160−18173

problems can be traced back to the presence of unreacted Cd species in the starting (undoped) QD sample that lead to postgrowth of the QDs during the doping procedure due to the uncontrolled (and unwanted) addition of the Cd−Se units competing with the incorporation of Mn via desired addition of the Mn−Se units. We also demonstrate that the amount of remnant Cd anticorrelates with the abundance of secondary phosphine impurities in the reactants used in the synthesis of the original CdSe QDs. A further identified challenge is the inability of standard purification techniques to fully remove unreacted Cd species due to their poor solubility in either polar or nonpolar solvents.

To tackle the above problems, we modified the CdSe QDs synthesis by adding controlled amounts of secondary phosphines in the form of DPP, which allowed us to reduce the abundance of remnant Cd in the reaction products from 75% to 25% of the original amount in the Cd precursor. In addition, we revised the purification procedure by adding a step of treatment with OA which helps solubilize the unreacted Cd species. These two alterations allow us to achieve a virtually complete suppression of QD postgrowth and realize a nearly ideal doping reaction which proceeds solely via addition of the Mn−Se species without a competing process of surface deposition of the Cd−Se units. Using this procedure, we greatly accelerate doping kinetics which allow us to achieve extra-high Mn contents (x_{Mn} > 30%) in a matter of just 15 min instead of multiple hours for standard doping techniques.

The high Mn contents are confirmed by low-temperature studies of magneto-optical properties of the doped QDs using MCD spectroscopy. The MCD measurements indicate that the developed doping method allows us to achieve doping levels that significantly exceed the point at which the concentration of isolated paramagnetic Mn ($x_{eff,Mn}$) is maximized and well into the high-doping regime where antiferromagnetic coupling between neighboring Mn spins becomes apparent in the magnetic and magneto-optical response. The corresponding peak value of $x_{eff,Mn} \approx 2\%$ is approximately half that in bulk semiconductor alloys which is a direct result of nonuniformity of the dopant distribution within the dot volume.

While, here, we have focused on the problem of QD diffusion doping, the insights gained from the conducted studies have broader implications and are applicable in other areas of QD chemistry involving postpreparation treatments of the QDs. In particular, the presence of unreacted metal-cation species may have an unpredictable (and likely deleterious) effect on cation exchange reactions often used for the preparation of core/shell structures and Janus particles as well as compositional conversion of the entire QD volume. Further, it may negatively affect ligand exchange reactions and follow-up assembly of the QDs into close-packed solids: the processing steps commonly applied during the fabrication of QD electronic and optoelectronic devices. The methods developed in the present study for detecting, quantifying, and controlling unreacted metal-cation species may help alleviate these problems and thereby allow for improvement in quality and, importantly, reproducibility of QD synthesis and device fabrication.

EXPERIMENTAL SECTION

Chemical and Materials. Cadmium oxide (CdO, Aldrich, 99.99%), octadecylphosphonic acid (ODPA, PCI, 99%), trioctylphosphine oxide (TOPO, Aldrich, 99%), trioctylphosphine (TOP, Aldrich, 90% or 97%), diphenylphosphine (DPP, Aldrich, 98%), selenium (Se, Alfa Aesar, 200 mesh, 99.999%), 1-octadecene (ODE, Aldrich, 90%), oleic acid (OA, Aldrich, 90%), oleylamine (Aldrich, 70%), manganese(II) acetate tetrahydrate ($Mn(ac)_2{\cdot}4H_2O$, Strem, 99.999%), and tributylphosphine (TBP, Aldrich, 95%) were used as received.

General Considerations. All syntheses of QDs were carried out under N_2 atmosphere in a three-neck flask attached to a standard Schlenk line setup. Washing and rinsing of the QDs after the synthesis as well as after the completion of the doping reaction were performed under ambient conditions.

QD Synthesis. To synthesize wurtzite CdSe QDs, we followed a previously reported method with some modifications.[34,35] CdO (60 mg), ODPA (280 mg), and TOPO (3 g) were loaded in a 50 mL 3-neck flask and heated to 150 °C under vacuum for 1 h. The temperature was increased to 320 °C under a N_2 atmosphere, and the mixture was maintained at this temperature until it turned into a transparent solution (stage 1). TOP (1.8 mL) was swiftly injected at 320 °C (stage 2). The temperature was further increased to 380 °C, and TOP-Se (0.433 mL of TOP and 0.058 g of Se) was swiftly injected (stage 3). After waiting for 1 min at 380 °C for full growth (stage 4), the solution was cooled down to room temperature by removing the heating mantle.

To improve Cd consumption, we modified the above synthesis by introducing DPP in the growth reaction. Controlled molar amounts of DPP were added to TOP of 97% purity at either stage 2 or both stages 2 and 3.

QD Purification with Oleic Acid. For a more complete removal of unreacted Cd species, the preformed QD samples were treated with OA (Figure S3). During this procedure, the CdSe QDs were first precipitated with ethanol; the precipitate was dissolved in toluene, and the solution was precipitated again with ethanol. Afterward, the QD precipitate was added to the mixture of degassed ODE (3 mL) and OA (0.3 mL) prepared in a 25 mL three-neck flask. The mixture was heated to 60 °C under vacuum for 1 h. Then, the QDs were purified again using a solvent/nonsolvent procedure following the same protocol as the one used prior to the OA treatment. The purified QDs were mixed with TBP-Se in ODE and used in the doping reaction as described below.

Doping of Preformed QDs with Manganese. To incorporate manganese in the preformed CdSe QDs, we applied a diffusion doping procedure from ref 34. Specifically, ODE (5 mL), oleylamine (0.433 mL), OA (0.20 mL), and $Mn(ac)_2{\cdot}4H_2O$ (10 mg) were loaded in a 3-neck flask and heated to 100 °C under vacuum for 1 h. The temperature was increased to 300 °C, and CdSe QDs (8.3 mg) and TBP-Se in ODE mixture (0.667 mL) were swiftly injected. The mixture was prepared by rinsing CdSe QDs with ethanol several times and then mixing them with Se (170 mg), TBP (5 mL), and ODE (5 mL) in a glovebox. After injection of the QDs and Se mixture solution, the temperature was kept 300 °C for a desired reaction time. Then, the solution was cooled down to room temperature by removing the heating mantle.

Elemental Analysis. To determine Mn content in the fabricated $Cd_{1-x}Mn_xSe$ QDs, we applied ICP-AES measurements using a Shimadzu ICPE-9000 inductively coupled plasma-atomic emission spectrometer. For these measurements, the QDs were rinsed with methanol five times and digested in a 1% HNO_3 solution in deionized water.

Optical Characterization. Absorption spectra of the fabricated undoped and Mn-doped QDs were measured using an Agilent Cary 8454 UV−vis spectrophotometer. The QD samples were prepared as dilute hexane solutions in a quartz cuvette with a 1 mm thickness, which defined the length of the optical path.

NMR Spectroscopy. NMR measurements were conducted using a Bruker 400 MHz AVANCE NEO spectrometer. The ^{31}P spectra were referenced externally to phosphoric acid (0 ppm). The NMR data was collected using a standard ^{31}P pulse sequence with ^{1}H composite pulse decoupling, a 7.6 ms ^{31}P radiofrequency pulse for excitation, and 10 s delay for T_1 relaxation.

TEM Measurements. TEM studies were conducted using a JEOL 2010 microscope. The QD samples were rinsed with methanol five

https://dx.doi.org/10.1021/jacs.0c08510
J. Am. Chem. Soc. 2020, 142, 18160−18173

times and redispersed in hexane. Then, 10 μL of dilute QD solution in hexane were drop-casted onto a carbon-coated copper grid and dried.

Determination of QD Concentration. To determine QD concentration from eq 1, we used $\alpha_{1S,0}$ and Γ_{QD} obtained from the measured peak amplitude and the half-width of the band-edge 1S absorption feature, respectively. To determine σ_0, we utilized an empirical expression of ref 43, which related the 1S molar extinction coefficient ($\varepsilon_{1S,0}$) to the energy of the 1S transition (E_{1S})

$$\varepsilon_{1S,0}(M^{-1}cm^{-1}) = 1.55507 \times 10^5 + 6.67054 \times 10^{13}\exp[-E_{1S}(eV)/0.10551]$$

Using $\varepsilon_{1S,0}$, we found σ_0 from $\sigma_0(cm^{-2}) = 10^3\ln(10)(\varepsilon_{1S,0}/N_A)$. Finally, by comparing eq 1 of the present work with the empirical formula of ref 43 connecting the QD molar concentration (c_{QD}) with $\varepsilon_{1S,0}$ and the half-width of the 1S peak (Γ_{QD}) (eq 16 of ref 43), we obtained $(\pi\ln 2)^{-1/2}\Gamma_0 = 0.06$ eV, which yielded $\Gamma_0 = 0.0405$ eV.

MCD Measurements. The QD samples were mounted in a variable-temperature insert of a superconducting magnet with direct optical access and kept at a constant temperature of 2.75 K. A spectrally narrow probe light of a tunable wavelength was derived from a xenon arc lamp using a 300 mm scanning spectrometer. The probe light was mechanically chopped and also modulated between left- and right-circular polarizations by a photoelastic modulator (PEM). The probe beam was focused through the QD sample and was detected by an avalanche photodiode. The sum and the difference of the intensities of the transmitted probe light of the two opposite circular polarizations were measured using two separate lock-in amplifiers, one of which was synchronized to the mechanical chopper (sum signal) and the other to the PEM (difference signal). This allowed for simultaneous measurements of the spectrally resolved MCD signal and the absorbance of the samples. These measurements were performed in a magnetic field of up to 6 T applied along the probe propagation path (Faraday configuration). We calibrated the relationship between the measured MCD signal and $\Delta E_{Z,1S}$ by measuring the right- and left-circularly polarized absorption spectra of each sample at the highest magnetic field (6T), which provided a direct determination of $\Delta E_{Z,1S}$. From this calibration, $\Delta E_{Z,1S}$ can be inferred from all other MCD measurements at different applied fields and temperatures.

■ ASSOCIATED CONTENT

Supporting Information

The Supporting Information is available free of charge at https://pubs.acs.org/doi/10.1021/jacs.0c08510.

Derivation of Mn contents from the QD size analysis; band-edge absorption coefficients of size-uniform and polydisperse QD ensembles; approximate schemes of traditional and revised syntheses of undoped CdSe QDs; a protocol of CdSe QD purification employing treatment with oleic acid; additional absorption spectra of undoped and doped CdSe QDs prepared using three different batches of TOP; analysis of the effect of CdSe QD purification with oleic acid on doping efficiency; MCD measurements of Mn:CdSe QD samples prepared using a doping procedure of a varied duration (PDF)

■ AUTHOR INFORMATION

Corresponding Author

Victor I. Klimov − *Chemistry Division, Los Alamos National Laboratory, Los Alamos, New Mexico 87545, United States;* orcid.org/0000-0003-1158-3179; Email: klimov@lanl.gov

Authors

Ho Jin − *Chemistry Division, Los Alamos National Laboratory, Los Alamos, New Mexico 87545, United States; Center for High Technology Materials, University of New Mexico, Albuquerque, New Mexico 87131, United States;* orcid.org/0000-0001-7452-6791

Mateusz Goryca − *National High Magnetic Field Laboratory, Los Alamos National Laboratory, Los Alamos, New Mexico 87545, United States*

Michael T. Janicke − *Chemistry Division, Los Alamos National Laboratory, Los Alamos, New Mexico 87545, United States*

Scott A. Crooker − *National High Magnetic Field Laboratory, Los Alamos National Laboratory, Los Alamos, New Mexico 87545, United States;* orcid.org/0000-0001-7553-4718

Complete contact information is available at: https://pubs.acs.org/10.1021/jacs.0c08510

Notes

The authors declare no competing financial interest.

■ ACKNOWLEDGMENTS

The studies of manganese incorporation into QDs and structural and compositional characterization of the QD samples were supported by the Solar Photochemistry Program of the Chemical Sciences, Biosciences and Geosciences Division, Office of Basic Energy Sciences, Office of Science, U.S. Department of Energy. The characterization of magneto-optical properties of Mn-doped QDs was supported by the Laboratory Directed Research and Development program of Los Alamos National Laboratory (LANL) under project number 20200213DR. Measurements at the National High Magnetic Field Laboratory were supported by the National Science Foundation DMR-1644779, the State of Florida, and the U.S. Department of Energy.

■ REFERENCES

(1) Norris, D. J.; Efros, A. L.; Erwin, S. C. Doped Nanocrystals. *Science* **2008**, *319*, 1776−1779.

(2) Erwin, S. C.; Zu, L.; Haftel, M. I.; Efros, A. L.; Kennedy, T. A.; Norris, D. J. Doping Semiconductor Nanocrystals. *Nature* **2005**, *436*, 91−94.

(3) Beaulac, R.; Archer, P. I.; Ochsenvein, S. T.; Gamelin, D. R. Mn^{2+}-Doped CdSe Quantum Dots: New Inorganic Materials for Spin-Electronics and Spin-Photonics. *Adv. Funct. Mater.* **2008**, *18*, 3873−3891.

(4) Bussian, D. A.; Crooker, S. A.; Yin, M.; Brynda, M.; Efros, A. L.; Klimov, V. I. Tunable Magnetic Exchange Interactions in Manganese-Doped Inverted Core−Shell ZnSe−CdSe Nanocrystals. *Nat. Mater.* **2009**, *8*, 35−40.

(5) Yu, J. H.; Liu, X.; Kweon, K. E.; Joo, J.; Park, J.; Ko, K.; Lee, D. W.; Shen, S.; Tivakornsasithorn, K.; Son, J. S.; Park, J.; Kim, Y.; Hwang, G. S.; Dobrowolska, M.; Furdyna, J. K.; Hyeon, T. Giant Zeeman Splitting in Nucleation-Controlled Doped CdSe:Mn^{2+} Quantum Nanoribbons. *Nat. Mater.* **2010**, *9*, 47−53.

(6) Mikulec, F. V.; Kuno, M.; Bennati, M.; Hall, D. A.; Griffin, R. G.; Bawendi, M. G. Organometallic Synthesis and Spectroscopic Characterization of Manganese-Doped CdSe Nanocrystals. *J. Am. Chem. Soc.* **2000**, *122*, 2532−2540.

(7) Norris, D. J.; Yao, N.; Charnock, F. T.; Kennedy, T. A. High-Quality Manganese-Doped ZnSe Nanocrystals. *Nano Lett.* **2001**, *1*, 3−7.

(8) Baryshnikov, K. A.; Langer, L.; Akimov, I. A.; Korenev, V. L.; Kusrayev, Yu. G.; Averkiev, N. S.; Yakovlev, D. R.; Bayer, M. Resonant Optical Alignment and Orientation of Mn^{2+} Spins in CdMnTe Crystals. *Phys. Rev. B: Condens. Matter Mater. Phys.* **2015**, *92*, 205202.

(9) Fainblat, R.; Barrows, C. J.; Hopmann, E.; Siebeneicher, S.; Vlaskin, V. A.; Gamelin, D. R.; Bacher, G. Giant Excitonic Exchange

Splittings at Zero Field in Single Colloidal CdSe Quantum Dots Doped with Individual Mn^{2+} Impurities. *Nano Lett.* **2016**, *16*, 6371−6377.
(10) Ithurria, S.; Guyot-Sionnest, P.; Mahler, B.; Dubertret, B. Mn^{2+} as a Radial Pressure Gauge in Colloidal Core/Shell Nanocrystals. *Phys. Rev. Lett.* **2007**, *99*, 265501.
(11) Vlaskin, V. A.; Janssen, N.; Rijssel, J. v.; Beaulac, R.; Gamelin, D. R. Tunable Dual Emission in Doped Semiconductor Nanocrystals. *Nano Lett.* **2010**, *10*, 3670−3674.
(12) Chen, H.; Maiti, S.; Son, D. H. Doping Location-Dependent Energy Transfer Dynamics in Mn-Doped CdS/ZnS Nanocrystals. *ACS Nano* **2012**, *6*, 583−591.
(13) Yang, J.; Fainblat, R.; Kwon, S. G.; Muckel, F.; Yu, J. H.; Terlinden, H.; Kim, B. H.; Iavarone, D.; Choi, M. K.; Kim, I. Y.; Park, I.; Hong, H.; Lee, J.; Son, J. S.; Lee, Z.; Kang, K.; Hwang, S.; Bacher, G.; Hyeon, T. Route to the Smallest Doped Semiconductor: Mn^{2+}-Doped $(CdSe)_{13}$ Clusters. *J. Am. Chem. Soc.* **2015**, *137*, 12776−12779.
(14) Yang, J.; Muckel, F.; Baek, W.; Fainblat, R.; Chang, H.; Bacher, G.; Hyeon, T. Chemical Synthesis, Doping, and Transformation of Magic-Sized Semiconductor Alloy Nanoclusters. *J. Am. Chem. Soc.* **2017**, *139*, 6761−6770.
(15) Chen, H.; Chen, T.; Son, D. H. Measurement of Energy Transfer Time in Colloidal Mn-Doped Semiconductor Nanocrystals. *J. Phys. Chem. C* **2010**, *114*, 4418−4423.
(16) Sharma, V. K.; Guzelturk, B.; Erdem, T.; Kelestemur, Y.; Demir, H. V. Tunable White-Light-Emitting Mn-Doped ZnSe Nanocrystals. *ACS Appl. Mater. Interfaces* **2014**, *6*, 3654−3660.
(17) Huang, B.; Dai, Q.; Zhuo, N.; Jiang, Q.; Shi, F.; Wang, H.; Zhang, H.; Liao, C.; Cui, Y.; Zhang, J. Bicolor Mn-Doped $CuInS_2$/ZnS Core/Shell Nanocrystals for White Light-Emitting Diode with High Color Rendering Index. *J. Appl. Phys.* **2014**, *116*, 094303.
(18) Jo, D.; Kim, D.; Kim, J.; Chae, H.; Seo, H. J.; Do, Y. R.; Yang, H. Tunable White Fluorescent Copper Gallium Sulfide Quantum Dots Enabled by Mn Doping. *ACS Appl. Mater. Interfaces* **2016**, *8*, 12291−12297.
(19) Erickson, C. S.; Bradshaw, L. R.; McDowall, S.; Gilbertson, J. D.; Gamelin, D. R.; Patrick, D. L. Zero-Reabsorption Doped-Nanocrystal Luminescent Solar Concentrators. *ACS Nano* **2014**, *8*, 3461−3467.
(20) Wu, K.; Li, H.; Klimov, V. I. Tandem Luminescent Solar Concentrators Based on Engineered Quantum Dots. *Nat. Photonics* **2018**, *12*, 105−110.
(21) Singh, R.; Liu, W.; Lim, J.; Robel, I.; Klimov, V. I. Hot-Electron Dynamics in Quantum Dots Manipulated by Spin-Exchange Auger Interactions. *Nat. Nanotechnol.* **2019**, *14*, 1035−1041.
(22) Dong, Y.; Choi, J.; Jeong, H.; Son, D. H. Hot Electrons Generated from Doped Quantum Dots via Upconversion of Excitons to Hot Charge Carriers for Enhanced Photocatalysis. *J. Am. Chem. Soc.* **2015**, *137*, 5549−5554.
(23) Dong, Y.; Parobek, D.; Rossi, D.; Son, D. H. Photoemission of Energetic Hot Electrons Produced via Up-Conversion in Doped Quantum Dots. *Nano Lett.* **2016**, *16*, 7270−7275.
(24) Barrows, C. J.; Rinehart, J. D.; Nagaoka, H.; deQuilettes, D. W.; Salvador, M.; Chen, J. I. L.; Ginger, D. S.; Gamelin, D. R. Electrical Detection of Quantum Dot Hot Electrons Generated via a Mn^{2+}-Enhanced Auger Process. *J. Phys. Chem. Lett.* **2017**, *8*, 126−130.
(25) Beaulac, R.; Archer, P. I.; Liu, X.; Lee, S.; Salley, G. M.; Dobrowolska, M.; Furdyna, J. K.; Gamelin, D. R. Spin-Polarizable Excitonic Luminescence in Colloidal Mn^{2+}-Doped CdSe Quantum Dots. *Nano Lett.* **2008**, *8*, 1197−1201.
(26) Beaulac, R.; Schneider, L.; Archer, P. I.; Bacher, G.; Gamelin, D. R. Light-Induced Spontaneous Magnetization in Doped Colloidal Quantum Dots. *Science* **2009**, *325*, 973−976.
(27) Nelson, H. D.; Bradshaw, L. R.; Barrows, C. J.; Vlaskin, V. A.; Gamelin, D. R. Picosecond Dynamics of Excitonic Magnetic Polarons in Colloidal Diffusion-Doped $Cd_{1-x}Mn_xSe$ Quantum Dots. *ACS Nano* **2015**, *9*, 11177−11191.
(28) Rice, W. D.; Liu, W.; Baker, T. A.; Sinitsyn, N. A.; Klimov, V. I.; Crooker, S. A. Revealing Giant Internal Magnetic Fields Due to Spin Fluctuations in Magnetically Doped Colloidal Nanocrystals. *Nat. Nanotechnol.* **2016**, *11*, 137−142.
(29) Rice, W. D.; Liu, W.; Pinchetti, V.; Yakovlev, D. R.; Klimov, V. I.; Crooker, S. A. Direct Measurements of Magnetic Polarons in $Cd_{1-x}Mn_xSe$ Nanocrystals from Resonant Photoluminescence. *Nano Lett.* **2017**, *17*, 3068−3075.
(30) Gaj, J. A.; Grieshaber, W.; Bodin-Deshayes, C.; Cibert, J.; Feuillet, G.; d'Aubigné, Y. M.; Wasiela, A. Magneto-Optical Study of Interface Mixing in the CdTe-(Cd,Mn)Te System. *Phys. Rev. B: Condens. Matter Mater. Phys.* **1994**, *50*, 5512−5527.
(31) Cibert, J.; Scalbert, D. "Diluted Magnetic Semiconductors: Basic Physics and Optical Properties", In "*Spin Physics in Semiconductors*" ed. Dyakonov, M.; Springer: 2017.
(32) Shapira, Y.; Foner, S.; Ridgley, D. H.; Dwight, K.; Wold, A. Technical Saturation and Magnetization Steps in Diluted Magnetic Semiconductors: Predictions and Observations. *Phys. Rev. B: Condens. Matter Mater. Phys.* **1984**, *30*, 4021−4023.
(33) Dalpian, G. M.; Chelikowsky, J. R. Self-Purification in Semiconductor Nanocrystals. *Phys. Rev. Lett.* **2006**, *96*, 226802.
(34) Vlaskin, V. A.; Barrows, C. J.; Erickson, C. S.; Gamelin, D. R. Nanocrystal Diffusion Doping. *J. Am. Chem. Soc.* **2013**, *135*, 14380−14389.
(35) Carbone, L.; Nobile, C.; Giorgi, M. D.; Sala, F. D.; Morello, G.; Pompa, P.; Hytch, M.; Snoeck, E.; Fiore, A.; Franchini, I. R.; Nadasan, M.; Silvestre, A. F.; Chiodo, L.; Kudera, S.; Cingolani, R.; Krahne, R.; Manna, L. Synthesis and Micrometer-Scale Assembly of Colloidal CdSe/CdS Nanorods Prepared by a Seeded Growth Approach. *Nano Lett.* **2007**, *7*, 2942−2950.
(36) Liu, H.; Owen, J. S.; Alivisatos, A. P. Mechanistic Study of Precursor Evolution in Colloidal Group II−VI Semiconductor Nanocrystal Synthesis. *J. Am. Chem. Soc.* **2007**, *129*, 305−312.
(37) Peng, Z. A.; Peng, X. Nearly Monodisperse and Shape-Controlled CdSe Nanocrystals via Alternative Routes: Nucleation and Growth. *J. Am. Chem. Soc.* **2002**, *124*, 3343−3353.
(38) Owen, J. S.; Chan, E. M.; Liu, H.; Alivisatos, A. P. Precursor Conversion Kinetics and the Nucleation of Cadmium Selenide Nanocrystals. *J. Am. Chem. Soc.* **2010**, *132*, 18206−18213.
(39) Wang, F.; Buhro, W. E. Morphology Control of Cadmium Selenide Nanocrystals: Insights into the Roles of Di-*n*-octylphosphine Oxide (DOPO) and Di-*n*-octylphosphinic Acid (DOPA). *J. Am. Chem. Soc.* **2012**, *134*, 5369−5380.
(40) Barrow, C. J.; Chakraborty, P.; Kornowske, L. M.; Gamelin, D. R. Tuning Equilibrium Compositions in Colloidal $Cd_{1-x}Mn_xSe$ Nanocrystals Using Diffusion Doping and Cation Exchange. *ACS Nano* **2016**, *10*, 910−918.
(41) Pietryga, J. M.; Park, Y.-S.; Lim, J.; Fidler, A. F.; Bae, W. K.; Brovelli, S.; Klimov, V. I. Spectroscopic and Device Aspects of Nanocrystal Quantum Dots. *Chem. Rev.* **2016**, *116*, 10513−10622.
(42) Lee, Y. R.; Ramdas, A. K.; Aggarwal, R. L. Energy Gap, Excitonic, and "Internal" Mn^{2+} Optical Transition in Mn-Based II-VI Diluted Magnetic Semiconductors. *Phys. Rev. B: Condens. Matter Mater. Phys.* **1988**, *38*, 10600−10610.
(43) Jasieniak, J.; Smith, L.; Embden, J. v.; Mulvaney, P.; Califano, M. Re-Examination of the Size-Dependent Absorption Properties of CdSe Quantum Dots. *J. Phys. Chem. C* **2009**, *113*, 19468−19474.
(44) Wang, F.; Tang, R.; Buhro, W. E. The Trouble with TOPO; Identification of Adventitious Impurities Beneficial to the Growth of Cadmium Selenide Quantum Dots, Rods, and Wires. *Nano Lett.* **2008**, *8*, 3521−3524.
(45) Wang, F.; Tang, R.; Kao, J. L. -F.; Dingman, S. D.; Buhro, W. E. Spectroscopic Identification of Tri-*n*-octylphosphine Oxide (TOPO) Impurities and Elucidation of Their Roles in Cadmium Selenide Quantum-Wire Growth. *J. Am. Chem. Soc.* **2009**, *131*, 4983−4994.
(46) Joo, J.; Pietryga, J. M.; McGuire, J. A.; Jeon, S.; Williams, D. J.; Wang, H.; Klimov, V. I. A Reduction Pathway in the Synthesis of PbSe Nanocrystal Quantum Dots. *J. Am. Chem. Soc.* **2009**, *131*, 10620−10628.

https://dx.doi.org/10.1021/jacs.0c08510
J. Am. Chem. Soc. 2020, 142, 18160−18173

(47) Evans, C. M.; Evans, M. E.; Krauss, T. D. Mysteries of TOPSe Revealed: Insights into Quantum Dot Nucleation. *J. Am. Chem. Soc.* **2010**, *132*, 10973−10975.
(48) Steckel, J. S.; Yen, B. K. H.; Oertel, D. C.; Bawendi, M. G. On the Mechanism of Lead Chalcogenide Nanocrystal Formation. *J. Am. Chem. Soc.* **2006**, *128*, 13032−13033.
(49) Xi, L.; Tan, W. X. W.; Boothroyd, C.; Lam, Y. M. Understanding and Controlling the Growth of Monodisperse CdS Nanowires in Solution. *Chem. Mater.* **2008**, *20*, 5444−5452.
(50) Srivastava, O. K.; Secco, E. A. Studies on Metal Hydroxy Compounds. III. Thermal Analyses of Cadmium Derivatives $Cd(OH)_2$, CdOHCl, and CdOHF. *Can. J. Chem.* **1967**, *45*, 1375−1378.
(51) Muckel, F.; Yang, J.; Lorenz, S.; Baek, W.; Chang, H.; Hyeon, T.; Bacher, G.; Fainblat, R. Digital Doping in Magic-Sized CdSe Clusters. *ACS Nano* **2016**, *10*, 7135−7141.
(52) Furdyna, J. K. Diluted Magnetic Semiconductors. *J. Appl. Phys.* **1988**, *64*, R29−R64.
(53) Kuno, M.; Nirmal, M.; Bawendi, M. G.; Efros, A.; Rosen, M. Magnetic Circular Dichroism Study of CdSe Quantum Dots. *J. Chem. Phys.* **1998**, *108*, 4242.
(54) Archer, P. I.; Santangelo, S. A.; Gamelin, D. R. Direct Observation of sp−d Exchange Interactions in Colloidal Mn^{2+}- and Co^{2+}-Doped CdSe Quantum Dots. *Nano Lett.* **2007**, *7*, 1037−1043.

https://dx.doi.org/10.1021/jacs.0c08510
J. Am. Chem. Soc. 2020, 142, 18160−18173